

An Efficient Dual-reference Training Data Acquisition Method for CNN Image Super-Resolution

Yanhui Guo, Xiao Shu, and Xiaolin Wu, *Fellow, IEEE*

Abstract—For deep learning methods of image super-resolution, the most critical issue is whether the paired low and high resolution images for training accurately reflect the sampling process of real cameras. Low and high resolution (LR~HR) image pairs synthesized by existing degradation models (*e.g.*, bicubic downsampling) deviate from those in reality; thus the super-resolution CNN trained by these synthesized LR~HR image pairs does not perform well when being applied to real images. In this paper, we propose a novel method to capture a large set of realistic LR~HR image pairs using real cameras. The data acquisition is carried out under controllable lab conditions with minimum human intervention and at high throughput (about 500 image pairs per hour). The high level of automation makes it easy to produce a set of real LR~HR training image pairs for each camera. Our innovation is to shoot images displayed on an ultra-high quality screen at different resolutions. There are three distinctive advantages of our method for image super-resolution. First, as the LR and HR images are taken of a 3D planar surface (the screen) the registration problem fits exactly to a homography model and we can display specially designed markers on the image to improve the registration precision. Second, the displayed digital image file can be exploited as a reference to optimize the high frequency content of the restored image. Third, this high-efficiency data collection method makes it possible to collect a customized dataset for each camera sensor, for which one can train a specific model for the intended camera sensor. Experimental results show that training a super-resolution CNN by our LR~HR dataset has superior restoration performance than training it by existing datasets on real world images at the inference stage.

Index Terms—Super resolution, Convolutional neural network, Super-resolution datasets, Dual-reference training data

I. INTRODUCTION

Single image super-resolution (SR), the task of increasing the spatial resolution and details of a given image, has attracted great attention from the computer vision research communities in the last few decades [1]–[7]. In recent years, the state of the art of SR has been set and reset by various deep convolutional neural network (DCNN) based techniques [8]–[12]. In addition to the significant improvement in SR performance, these DCNN techniques also provide some important insights on the designs of DCNN architectures [13]–[20] and loss functions [21]–[24]. However, for any real-world problems, the efficacy of a machine learning technique relies not only on the design of the technique itself but also, sometimes even more critically, on the quality and representativeness of the training data.

As it is impossible to have real LR~HR image pairs, most existing SR techniques resort to synthetically generated low-resolution (LR) images for training. The overly-

simplistic downsampling operators commonly employed by these techniques, such as bicubic downsampling (BD) and Gaussian downsampling (GD), cannot accurately simulate the complex and compounded process of capturing a low-resolution image. When operating on real images, the DCNNs trained on these synthesized datasets generally cannot superresolve high frequency details to the same level of clarity and sharpness as when operating on synthetic LR images. This weakness of synthetic training images is well known to practitioners.

It is not easy to replace synthetic images with real ones in the training of SR networks. Capturing perfectly aligned real LR~HR image pairs is a highly challenging and expensive task. There have been a few attempts to collect datasets of paired LR and HR images [25]–[27]. Their basic idea is to capture each natural scene twice with lenses of different scale factors (focal lengths). Then, they form an image pair by aligning the two images using image registration techniques, possibly patch by patch. Although DCNNs trained with existing real datasets exhibit some improvement for certain types of real images, this real image collection approach is inherently problematic. Firstly, since each scene is captured twice, a scene has to be absolutely static between the two shots in order to avoid mismatches of the paired images. Thus, any moving subjects, such as animals or humans, cannot be included in the datasets. The restriction of no motions greatly narrows the scope of the training images. Secondly, registration errors caused by the perspective misalignment as demonstrated in Fig 1 and the different defocus blur effects of the two lenses could also lead to mismatches of LR and HR image pairs. These mismatches due to disparity are inevitable in scenes of depth variations. The lack of alignment precision between LR and HR training images can throw off the deep learning process, hindering the reconstruction of sharp image details.



Fig. 1: Illustration of the perspective misalignment of a paired LR~HR image from Cai *et al.* [26] after registration.

Except the aforementioned difficulties of the real SR datasets

collection, another thorny issue is that the real SR datasets are not camera-agnostic. This problem is caused by variant specifications (*e.g.* pixel pitch, noise model, sensitivity and *etc.*) of different camera sensors. These different factors could make the collected LR images obey a specific distribution which is highly dependent on the camera used for shooting. The SR DCNN trained with this camera-specific dataset thus inclines to overfit the camera and performs poorly outside the dataset. One simple way is to collect a large number of image pairs using all cameras for which the SR DCNN is designed. However, this is not practical, because collecting the diverse large dataset by shooting many scenes using different cameras is laborious and time consuming. Moreover, the SR DCNN trained by the mixed dataset will not yield the best results for a specific camera.

To circumvent the above difficulties, we propose a novel concept of SR training dataset of monitor-induced dual-reference paired images (MIDPI). The LR images X_i for training the SR network are real, physically acquired ones, rather than some algorithmically downsampled version of the corresponding HR image \mathcal{Y}_i (digital image file). The HR image \mathcal{Y}_i is displayed on an ultra-high resolution high-quality monitor; this displayed image is captured twice by a camera, in high resolution via a long focal lens, and also in low resolution via a short focal lens, generating the captured HR image Y_i and LR image X_i respectively. The (X_i, Y_i) image pair provides the deep learning SR network model with the information on pixel PSF, sensor noise statistics, lens characteristics, *etc.* These physical attributes are very difficult to model analytically as they are complex and compounded to each other; their effects on the SR task are best left for a data-driven CNN to factor in.

But the captured HR screen image Y_i by itself is not suited to be the ground truth, because it is not an exact copy of the original \mathcal{Y}_i . To compensate for this we also include \mathcal{Y}_i as a part of the ground truth, and introduce a new learning task of dual-reference SR, using the augmented training image data $(X_i, Y_i, \mathcal{Y}_i)$. In other words, the ground truth is now the dual references (Y_i, \mathcal{Y}_i) . The role of the original HR digital image \mathcal{Y}_i is to provide structural information on high frequency features that might be compromised by the analog operation of screen shooting. Fig. 2 illustrates the data collection process of MIDPI.

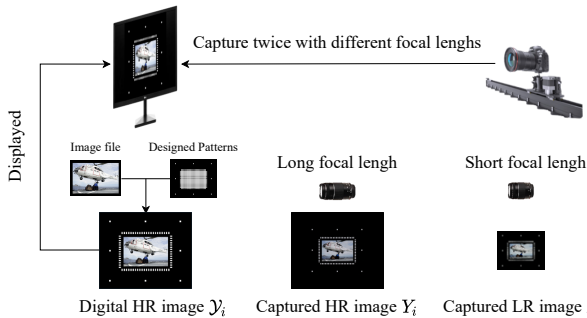


Fig. 2: Illustration of the data collection process of MIDPI.

The proposed process of shooting a ultra-high quality monitor to create paired LR~HR training images has a unique and big

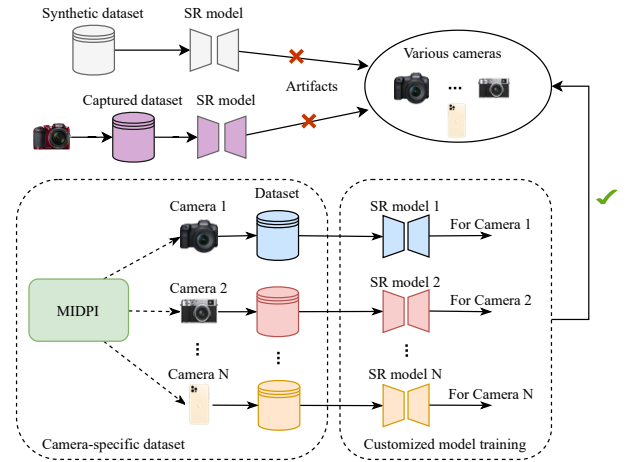


Fig. 3: The application of the proposed MIDPI.

advantage over the existing methods of shooting real LR~HR image pairs [26], [27]. That is, the former can achieve a much higher registration accuracy between the captured LR image X_i and the captured HR image Y_i ; and in turn, between X_i and \mathcal{Y}_i . Indeed, now our registration problem can be modeled exactly by homography transform for the screen image is a 3D planar surface. The flatness of the screen also prevents the problems of occlusion and defocusing due to depth disparity in pairing. In addition, as the scene of the captured image pairs is static, absolutely no object motions exist to cause spatially varying alignment parameters. To push the registration accuracy to the limit, we also display specially designed registration markers on the screen. These markers are used to align LR~HR image pairs to sub-pixel precision by frequency and phase estimation techniques.

The screen shooting is carried out in a controlled dark room lab. environment to eliminate ambient lights. The camera sensor projection plane is calibrated to align with and have sufficient distance from the screen surface to prevent moire interferences and geometric distortions. Finally, the training image acquisition and pairing process is carefully designed so that even if a small registration error exists, the error will be the same for all LR~HR image pairs. This small constant error in registration will only cause an indiscernible shift of the reconstructed HR image from \mathcal{Y}_i , but not blurring artifacts.

Another advantage of the proposed LR~HR image data collection procedure is its scalability to data volume. Once the shooting environment is setup, the whole procedure, including capturing and alignment, can be easily automated without manual intervention. The data collection throughput can reach 500 image pairs per hour. Moreover, the same procedure can be conveniently and quickly repeated for different cameras. This allows the creation of a large training dataset dedicated to a specific camera with ease, opening up the possibility to optimize a SR CNN method for each camera *i.e.* a camera-specific model, to achieve the best performance, as illustrated in Fig 3. In contrast, all previous methods of shooting real LR~HR image pairs are highly laborious and very expensive, not scalable to the size of training datasets nor to the number of different cameras.

II. RELATED WORK

There are several popular datasets that have been extensively used for training and testing in SR, such as Set5 [28], Set14 [29], Urban100 [6] and DIV2K [30]. In all of these datasets, the LR images were generated from the HR images via synthetic degradation like bicubic downsampling or Gaussian blurring followed by direct downsampling [31]. Xu *et al.* [32] proposed a method to generate approximate realistic training data by simulating the imaging process of digital cameras. Yoo *et al.* [33] proposed a CutBlur method to augment training data for super-resolution. Jeon *et al.* [34] and Wang *et al.* [35] tried to improve super-resolution performance by using stereo low resolution images. Besides, Generative adversarial networks (GANs) have also been applied to generate realistic degraded images [36]–[38]. Nevertheless, all these synthetic datasets are still far away from the real images.

Recently, some researchers have attempted to capture real-world image pairs for SR. Qu *et al.* [39] obtained paired LR~HR images by placing a beam splitter in the optical path of two identical camera sensors. But their dataset only includes face images. Köhler *et al.* [40] implemented hardware binning on the sensors to collect real data, but it only has 14 scenes. Zhang *et al.* [27] collected 500 scenes using multiple focal lengths. However, they cannot register the paired images precisely because of perspective misalignment. Chen *et al.* [25] printed 100 images to postcards and captured LR~HR image pairs, but the models trained on this dataset cannot generalize well to real-world scenes and they cannot register the image pairs precisely by only using SIFT [41] features. Cai *et al.* [26] collected 595 LR~HR image pairs using two digital single-lens reflex (DSLR) cameras. However, they meet the perspective misalignment as same as [27] and they cannot capture paired data from dynamic scenes. Different from them, our MIDPI system can automatically generate enough precisely aligned LR~HR image pairs at a low cost.



Fig. 4: Illustration of the MIDPI system employed in our experiment.

III. METHOD

In this section, we present the details of the proposed procedure of generating SR training datasets of monitor-induced dual-reference paired images (MIDPI).

A. Images capture system

1) *System hardware*: Fig. 4 shows the controlled laboratory setting for the MIDPI data acquisition. We collect MIDPI

TABLE I: Camera configuration and the number of captured image pairs.

Camera	Sony Nex-6	Canon 5D-MarkIII	Sony Alpha-a7RII
Aperture	f/10	f/10	f/10
Shutter speed	1/30s	1/50s	1/30s
Focal length	18mm&80mm	30mm&120mm	18mm&80mm
Pixel pitch	4.8 μ m	6.2 μ m	6.0 μ m
Pixel area	22.75 μ m ²	38.69 μ m ²	20.25 μ m ²
Distance	5.3m	6.2m	4.3m
Image pairs	600	600	600

training data by shooting natural images displayed on a 4K UHD (3840 \times 2160) HDR10 monitor by a digital camera. We obtain LR images with short focal lens and HR images with long focal lens. To prevent blur caused by possible vibrations of the camera, we mount the camera on a track dolly slider and trigger the shutter using a WiFi remote controller. Three cameras, Sony Nex-6, Canon 5D-MarkIII and Sony Alpha-a7RII, are used to increase the variety of camera statistics in reality.

2) *Setup of acquisition system*: To prevent possible moiré patterns in captured screen images, the camera should be placed at a sufficient distance from the monitor. We denote the focal length of the camera, the object distance and the pixel pitch of the screen by f , d and u_s respectively. The size of an imaged pixel on screen through the lens is

$$u_i = u_s \frac{f}{d} \quad (1)$$

Moiré patterns are caused by the interference between the screen image and the color filter array of the camera. By the Nyquist–Shannon sampling theorem, moiré patterns can be eliminated if the camera sensor sampling step size $u_c > 2u_i$. Then it follows from Eq. 1 that the moiré-free distance between the camera and the screen is

$$d > 2f \frac{u_s}{u_c} \quad (2)$$

As the focal length for capturing LR images is shorter than the focal length for HR images, eliminating moiré patterns in captured HR images will also ensure no moiré patterns in LR images. Therefore we determine the camera position by the long focal length for capturing HR images. In addition, to simplify the LR~HR registration, we set the focal plane (sensor array) of the camera parallel to the screen surface. To achieve this we display a square pattern on the screen, and make sure the pattern to remain a square in the captured screen image, by adjusting the universal angle plate on which the camera is mounted.

3) *Data collection process*: We conduct multiple shooting sessions using three cameras to ensure a sufficiently large data volume and diversity to facilitate deep learning. The camera specifications and settings for the data acquisition process are tabulated in Table I. To keep the consistency of each captured LR~HR image pair (X_i, Y_i), we only change the focal length of the lens once for each camera. More specifically, We first capture all needed LR images with the same short focal length, then we adjust the focal length and capture the corresponding HR images. This can reduce the registration error caused by

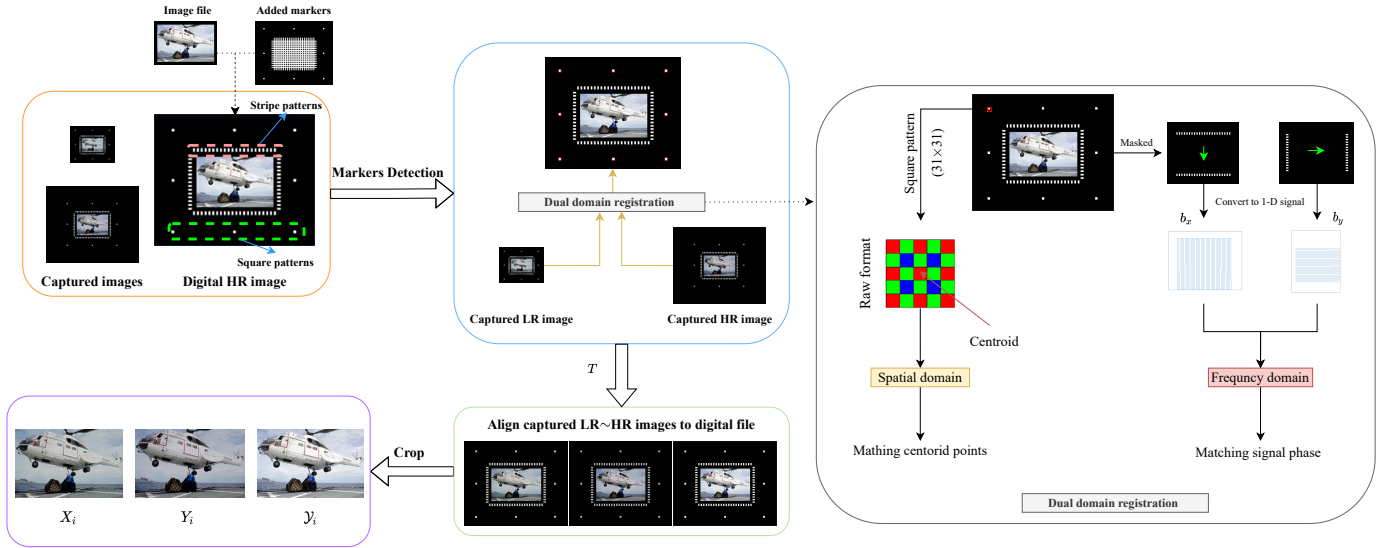


Fig. 5: Overall process of the image registration between the captured LR image X_i and the captured HR image Y_i . The captured LR image X_i and the captured HR image Y_i are aligned to the digital image \mathcal{Y}_i .

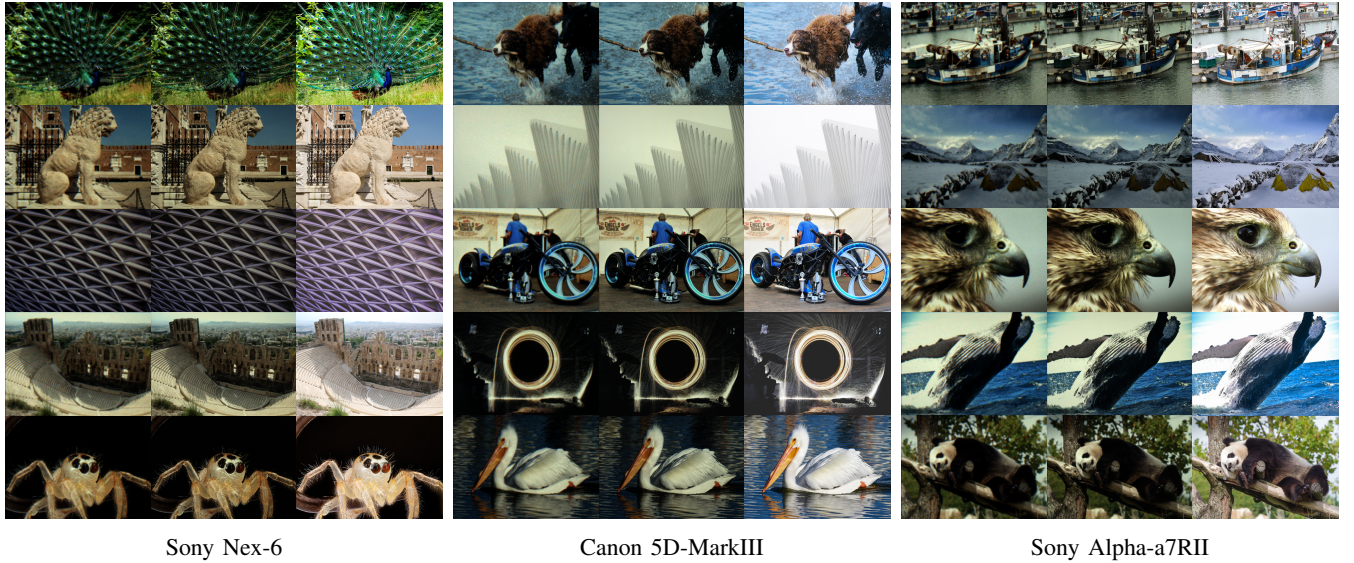


Fig. 6: Samples of the collected LR~HR image pairs in MIDPI. In each sample, the captured LR image X_i is placed on the left, the captured HR image Y_i is placed on the middle and the digital HR image \mathcal{Y}_i is placed on the right.

the frequent mechanical changes. During the dataset collection process, we simultaneously save the displayed digital image \mathcal{Y}_i .

To remove all unnecessary variations among acquired images, all camera parameters irrelevant to spatial resolution, such as white balance, aperture size and exposure time, should be fixed. We thus collect raw Bayer images rather than JPEG images produced by the camera built-in image processing pipeline. The LR and HR raw Bayer images are demosaiced into corresponding RGB images of linear scale without any tone mapping nor gamma correction. We correct the lens distortion with Zhang's method [42]. To factor out the influences of monitor backlight, we display a black image on the monitor at the beginning of every shooting process and subtract it from every captured image afterwards. The ultra-high quality

monitor and the DSLR camera are remotely operated in a dark room so as to prevent any interference of ambient light and any motions of the monitor and camera.

B. LR~HR registration

In the MIDPI system, the images are displayed on a flat monitor. This advantage inherently eliminates the noticeable perspective misalignment of LR~HR images caused by the depth disparity when capturing real scenes [26], [27]. In addition, after the pre-calibration by making the camera parallel to the monitor surface, the transformation matrix between the LR~HR image pair is simplified to an affine transformation matrix T . To estimate the affine transformation, some popular keypoints based image registration algorithms, such as SIFT

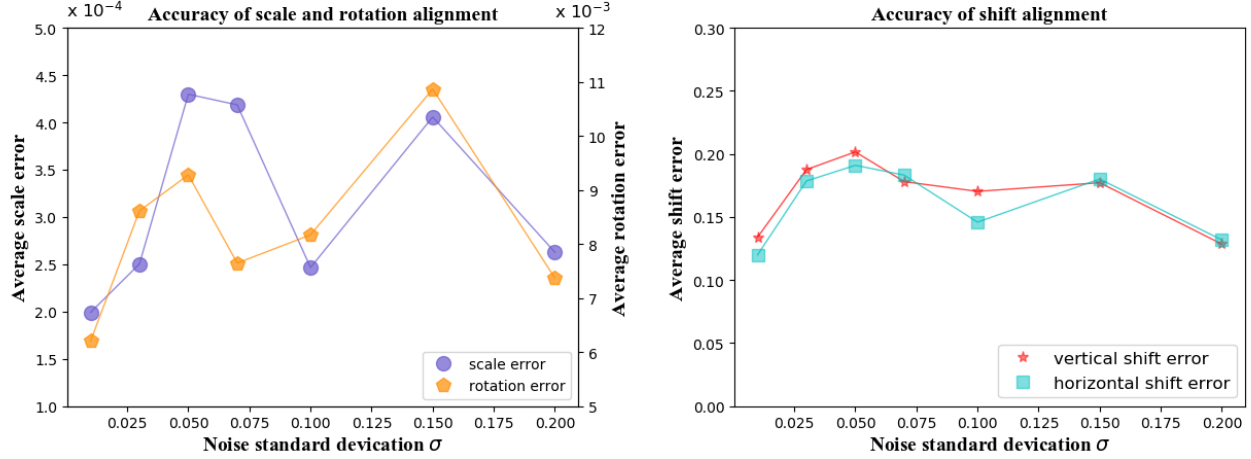


Fig. 7: Accuracy of the proposed image alignment algorithm in aligning randomly scaled, rotated and shifted images.

[41] and SURF [43], work well, but these general keypoints based methods cannot support accurate pixel-wise registration, let alone sub-pixel level.

To achieve robust and highly accurate LR~HR registration, we design special patterns and the digital file is embedded in these patterns to be displayed on the screen, as shown in the left of Fig. 5. Two sets of patterns are used to support a novel LR~HR registration method in dual spatial and frequency domains to be detailed later. The first set consists of eight solid square patterns, four at the corners of the image, and the other four at the center of the four sides of the image. These eight markers are for LR~HR registration in spatial domain. The second set consists of horizontal bars and vertical bars of fixed frequencies. These bar patterns are used for LR~HR registration in frequency domain.

To register dual reference training data, we align both the captured LR image X_i and the captured HR image Y_i to the displayed digital image \mathcal{Y}_i . To keep the training data same resolution, we upsample X_i and downsample \mathcal{Y}_i to the size of Y_i . Next, for simplicity, we introduce the registration process of (X_i, \mathcal{Y}_i) , the same to (Y_i, \mathcal{Y}_i) . Fig 5 illustrates the overall registration process in MIDPI. Firstly, we detect all the solid square patterns and crop valid content regions of LR~HR. For each square pattern, we calculate the centroid as a matching point for image alignment in spatial domain. The calculated centroid is of sub-pixel accuracy and robust to align the LR~HR image pair regardless of the blur and noise of the images. To achieve higher precision of the computed centroid, the centroid calculation is computed using the raw Bayer format data. However, due to the inconsistent sensitivity of the color filter array for different colors, it will bring errors to the centroid estimation, as depicted in Figure 9. To prevent this, before the centroid calculation, we calibrate the difference of the color sensitivity of each channel and reweight the color channels to a same sensitivity level. Denote the detected area of k -th square pattern by $\Omega_k(x, y)$, the k -th matching point of

LR image is

$$(\bar{x}_k, \bar{y}_k) = \left(\frac{\sum_x \sum_y x \Omega_k(x, y)}{|\Omega_k(x, y)|}, \frac{\sum_x \sum_y y \Omega_k(x, y)}{|\Omega_k(x, y)|} \right) \quad (3)$$

To match the corresponding centroid point (u_k, v_k) of the digital HR image \mathcal{Y}_i , our method minimizes the following objective function with homogeneous coordinate representation:

$$\min_T \left\| T \begin{bmatrix} \bar{x}_1 & \cdots & \bar{x}_8 \\ \bar{y}_1 & \cdots & \bar{y}_8 \\ 1 & \cdots & 1 \end{bmatrix} - \begin{bmatrix} u_1 & \cdots & u_8 \\ v_1 & \cdots & v_8 \\ 1 & \cdots & 1 \end{bmatrix} \right\|_F \quad (4)$$

We thus can get $T = BA^T(AA^T)^{-1}$. The centroid based image registration can quite precisely align the scale and the rotation of the image pair, however there is still room for the improvement to align the shift between the image pair by *e.g.* phase registration.

Algorithm 1 Maximum Peak Frequency Search Algorithm

Require: The 1D bar signal, b ;

Require: The search scope, δ ; The step size, τ ;

1: Initialize peak frequency $w_0 \leftarrow \underset{w}{\operatorname{argmax}} |\operatorname{FFT}(b)|$

2: Maximum similarity $\tilde{s} \leftarrow 0$

3: $w \leftarrow w_0 - \delta$

4: **while** $w < w_0 + \delta$ **do**

5: $s \leftarrow |\langle b, e^{j2\frac{\pi}{N}w} \rangle|$

6: **if** $\tilde{s} < s$ **then**

7: $\tilde{s} \leftarrow s$

8: $\tilde{w} \leftarrow w$

9: **End if**

10: $w \leftarrow w + \tau$

11: **End while**

Output: \tilde{w}

Thanks to the MIDPI system by capturing the monitor, we can purposefully design periodic bar patterns, as shown in

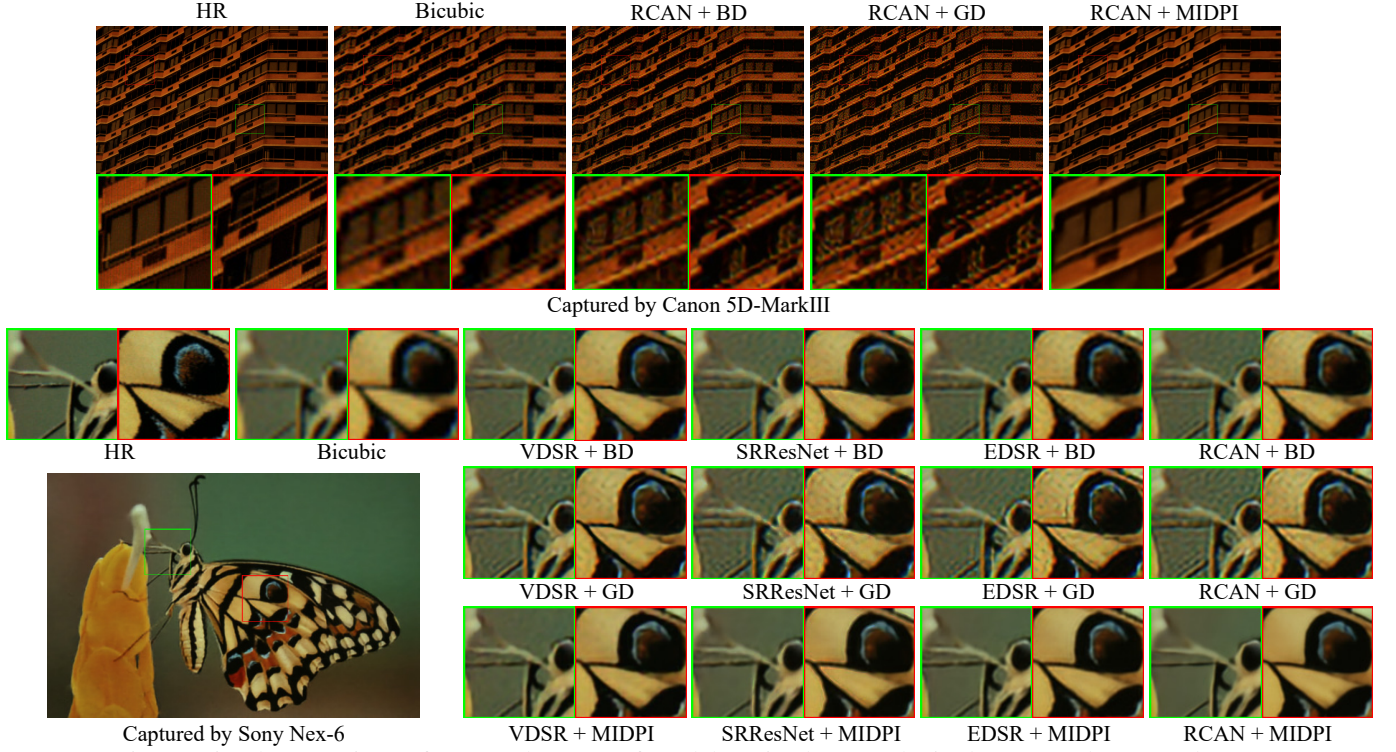


Fig. 8: Visual comparison of SR results ($\times 4$) of models trained on synthetic datasets and MIDPI dataset.

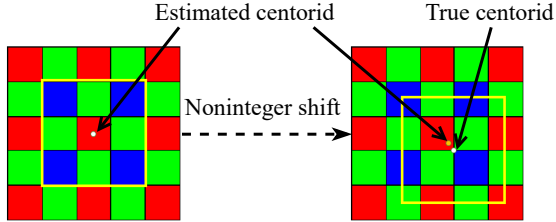


Fig. 9: Illustration of the centroid calculation in the raw format. The left shows the centroid can be estimated correctly when the yellow block overlaps the color array perfectly. But when the shift is non-integer, the estimated centroid may deviate from the true centroid.

the right of Fig 5, to match the phase of the specific patterns in frequency domain rather than the popular general phase registration [44]. First, we mask the image and extract the orthogonal bar patterns for horizontal shift registration and vertical shift registration respectively. Then we can project these 2D bar patterns to 1D square wave signals along the vertical direction and horizontal direction. Denote the horizontal signal with length N_x and the vertical signal with length N_y by b_x and b_y of the image X_i . The counterparts of the image \mathcal{Y}_i are b_x^c and b_y^c . The phase difference of the paired square wave signals accurately represents the pixel shift between the 2D bar patterns, theoretically of which the precision can achieve an arbitrary fraction of a pixel [45]. To estimate the phase differences between the paired signals, we first project b_x and b_y to the first harmonics $e_{w_x} = e^{j2\frac{\pi}{N_x}w_x}$ and $e_{w_y} = e^{j2\frac{\pi}{N_y}w_y}$, where w_x and w_y represent the fundamental frequencies of b_x and b_y respectively and j is the imaginary unit. The projection

computation is defined as following

$$e_x = \frac{\langle b_x, e_{w_x}^* \rangle}{|\langle b_x, e_{w_x}^* \rangle|}, \quad e_y = \frac{\langle b_y, e_{w_y}^* \rangle}{|\langle b_y, e_{w_y}^* \rangle|} \quad (5)$$

where $*$ is the conjugate transpose and $\langle \cdot \rangle$ is the inner product. Similarly, the projected signals c_x and c_y of the digital image \mathcal{Y}_i can be computed. We denote the fundamental frequencies of b_x^c and b_y^c by w_x^c and w_y^c respectively. The maximum peak frequencies *i.e.* the fundamental frequencies can be calculated by FFT, however, the discrete fourier transform can only provide integer frequency which is not enough for sub-pixel alignment. We thus further use a finer search method (see Algorithm 1) to pinpoint the fundamental frequencies. We set the search bound $\delta = 1$ and the step size $\tau = 0.001$. With the accurate estimated frequencies, we can precisely compute the horizontal pixel shift u_x derived from the phase difference of e_x and c_x and the vertical pixel shift u_y derived from the phase difference of e_y and c_y as following

$$t_x = \left(\frac{\Phi(e_x)}{2\pi w_x} - \frac{\Phi(c_x)}{2\pi w_x^c} \right) N_x, \quad t_y = \left(\frac{\Phi(e_y)}{2\pi w_y} - \frac{\Phi(c_y)}{2\pi w_y^c} \right) N_y \quad (6)$$

where $\Phi(\cdot)$ represents the phase angle computation. With the estimated translations, we align the captured LR image X_i to the digital image \mathcal{Y}_i .

C. Dual reference loss function

In MIDPI system, except the camera captured HR images Y_i , we have super high-quality reference images *i.e.* digital file \mathcal{Y}_i . Compared to this digital file, the camera captured Y_i may suffer from loss of high frequency features. This motivates us to supervise the SR model training by using both Y_i and

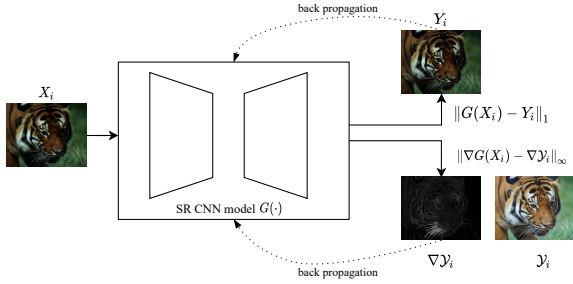


Fig. 10: Illustration the training process with MIDPI data.

digital file \mathcal{Y}_i . To this end, we proposed a dual reference loss function:

$$\mathcal{L}(G(X_i), Y_i, \mathcal{Y}_i) = \|G(X_i) - Y_i\|_1 + \lambda \|\nabla G(X_i) - \nabla \mathcal{Y}_i\|_\infty \quad (7)$$

where $G(\cdot)$ represents an arbitrary SR CNN model, ∇ is a differential operator and λ is a trade-off weight. The former ℓ_1 -norm term minimizes the pixel-wise error between the prediction $G(X_i)$ and the captured HR image Y_i . In addition, we introduce a regulation term to enforce the gradient similarity between the prediction $G(X_i)$ and the digital HR image \mathcal{Y}_i , improving the high frequency textures of the prediction $G(X_i)$. To avoid producing over-smooth results, we adopt an infinite norm. By minimizing the dual reference loss function $\mathcal{L}(G(X_i), Y_i, \mathcal{Y}_i)$, the pixel PSF between X_i and Y_i and the high frequency information of \mathcal{Y}_i can be jointly learned by a SR CNN model in an end-to-end manner, as illustrated in Fig 10.

IV. EXPERIMENTAL RESULTS

As reported in Table. I, to build the MIDPI datasets, we collect 1800 paired images from three DSLR cameras. For each MIDPI dataset (Sony Nex-6 MIDPI dataset, Canon 5D-MarkIII MIDPI dataset and Sony Alpha-a7RII MIDPI dataset), we randomly select one tenth of the number of image pairs to form test dataset, while using the rest of image pairs for training. In this section, we use the Sony Nex-6 MIDPI dataset to examine the differences between models trained on synthetic datasets and the MIDPI dataset. Moreover, we are more interested in the performance and generalization of the MIDPI-trained model for real scenes. For this purpose, we conduct an evaluation of real scenes and all images of three MIDPI datasets are used for model training. Because of the various degradation produced by the camera lens and sensors, the MIDPI-trained models are not device-free. To measure this diffidence, we conduct a cross-camera test. Following previous work [12], [15], [17], quantitative metrics PSNR and SSIM are calculated on the Y channel in the YCbCr space.

In the training process, we randomly crop the training images into 256×256 patches to train all the models and the mini-batch size in all the experiments is set to 8. The trade-off weight λ is set 0.1. Adam optimizer [46] is chosen to train all models by setting initial learning rate 10^{-4} . The learning rate is fixed in first 10K iterations and linearly decay to 10^{-6} after 70K iterations. With same parameters setting, all the experiments are conducted on a PC with single NVIDIA TITAN XP GPU.

A. Evaluation of proposed dual domain registration method

In this section, we evaluate the precision of the image pair registration method in MIDPI system. In Fig. 7, we show an evaluation study of the image alignment method proposed in Sec III-B. In this experiment, we prepare 500 images with the the designed patterns. For each of the image, we first downsample it by a random scale factor between 0.3 to 1, then shift it randomly in both horizontal and vertical directions by $-5 \sim 5$ pixels and finally randomly rotate them between -3 to 3 degrees. Please note that the shift and rotation amount is not necessarily integer. To evaluate the robustness of the proposed image alignment method, the resulting resampled image is added with zero mean Gaussian noises of various standard deviations $\sigma \in \{0.01, 0.03, 0.05, 0.07, 0.1, 0.15, 0.2\}$ and fed to the proposed alignment method. As plotted in Fig. 7, the estimated shifts of the image are off by less than 0.2 pixel error on average in comparison with the ground truth; and the errors of the estimated scale and the estimated rotation are negligible. Moreover, the proposed image registration method performs well and stably in aligning the images with varouse noise levels.

B. Results of laboratory datasets

The ultimate criterion of success for the proposed MIDPI data collection procedure is whether the MIDPI-trained DCNN model for super resolution can indeed outperform the counterpart trained by other LR~HR datasets when both being applied to infer on real world images. But for the sake of completeness and reference purpose, let us first evaluate the inference results on MIDPI data. We compare how a given DCNN SR model performs when it is trained by different datasets, including both synthesized and MIDPI. In the comparison study, two synthetic LR~HR datasets, denoted by BD and GD, are generated by downsampling the captured HR images Y_i of the MIDPI dataset using bicubic and Gaussian kernels. To fairly evaluate the difference between the synthetic datasets and our real captured MIDPI dataset, in this experiment, all MIDPI-trained DCNN models are supervised by the captured image pairs (X_i, Y_i) . Table. II reports the PSNR and SSIM values (with scaling factor $\times 4$) of different SR models VDSR [20], SRResNet [22], EDSR [15], RCAN [17] after trained by different datasets.

As reported in Table. II, for each of the five tested SR methods, the MIDPI-trained model has significant improvement over the BD-trained model and the GD-trained model, with gains from 1.7dB to 2.5dB. The visual quality comparison is presented in Fig. 8. As shown, the SR results associated with the training datasets BD and GD have more artifacts and more blurred edges than with the MIDPI dataset. It is expected that our MIDPI dataset outperforms BD and GD, because it characterizes statistical relations between the LR and HR images more accurately for the camera.

C. Results of superresolving real world images

Our MIDPI training dataset distinguishes itself from previous camera-acquired training datasets (e.g. [26], [27]) for the SR task in that it has much higher sub-pixel precision of LR~HR

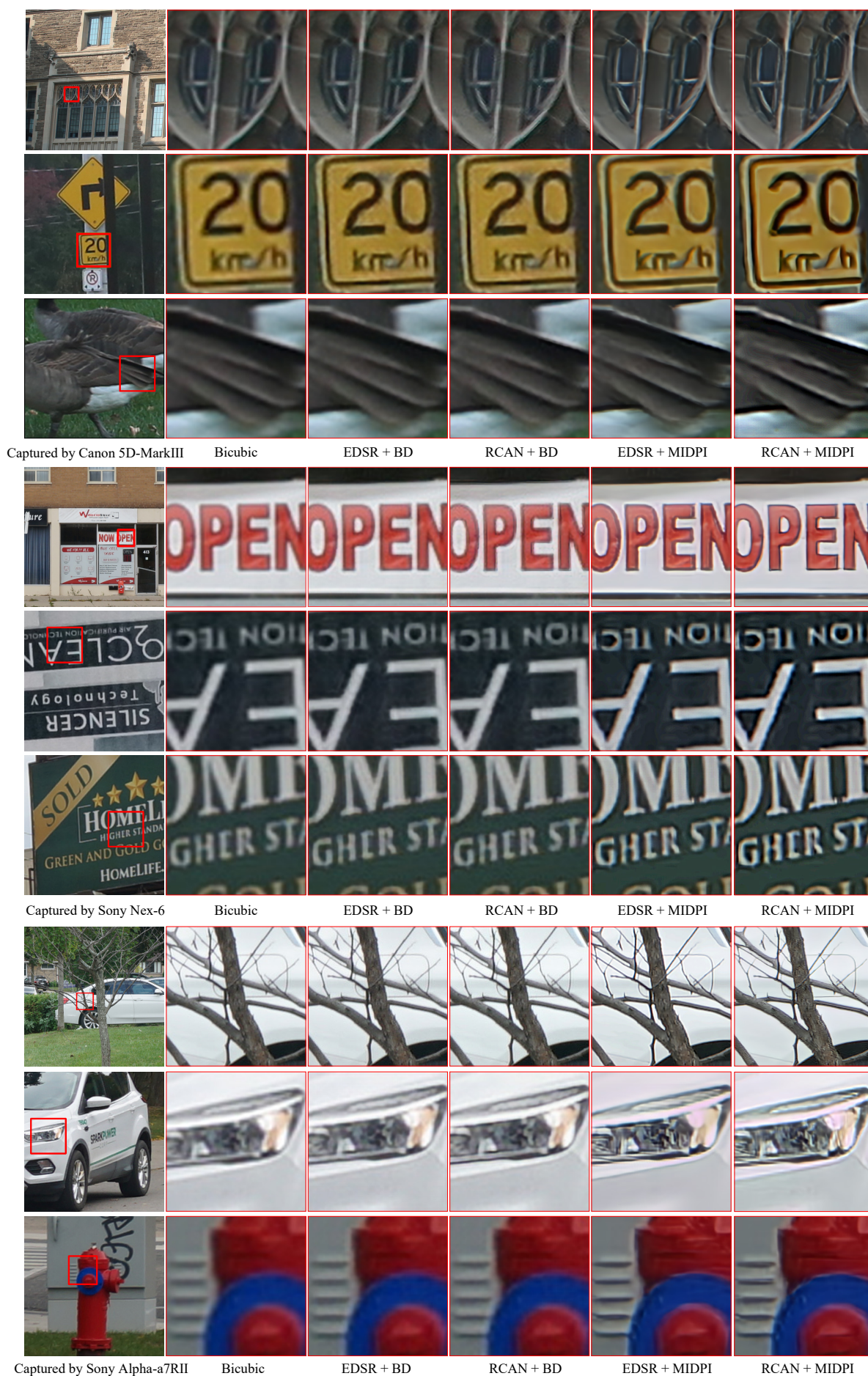


Fig. 11: SR results ($\times 4$) of real-world images outside our dataset. Zoom in for better view.

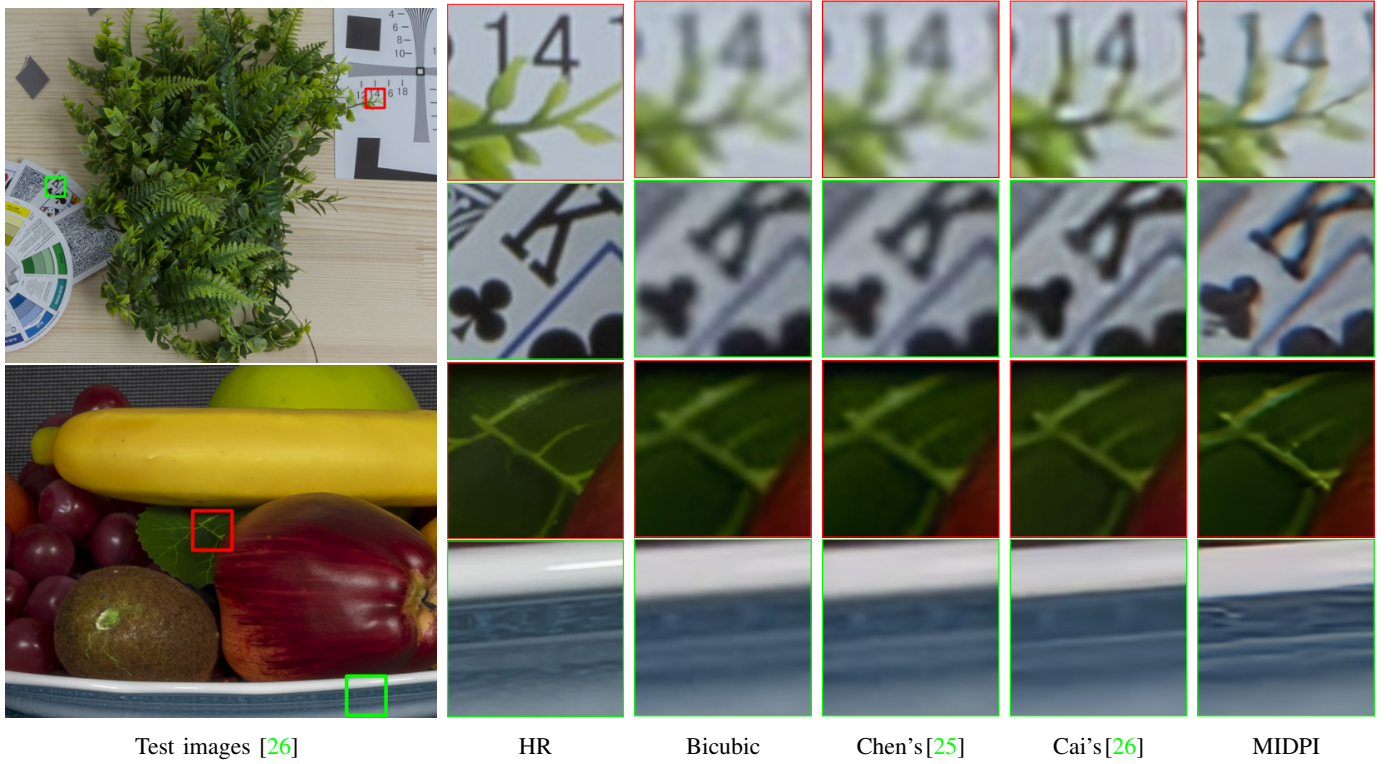


Fig. 12: SR results ($\times 4$) of real-world images from Cai's [26]. All models are of RCAN structure.

TABLE II: The comparison of different state-of-the-art methods trained on the synthetic datasets and the MIDPI dataset.

Methods ($\times 4$)	BD		GD		MIDPI	
	PSNR	SSIM	PSNR	SSIM	PSNR	SSIM
Bicubic	29.26	0.811	29.26	0.811	29.26	0.811
VDSR	30.41	0.838	30.64	0.841	32.12	0.860
SRResNet	30.51	0.837	30.59	0.836	32.53	0.871
EDSR	30.68	0.838	30.65	0.838	32.57	0.871
RCAN	30.78	0.842	30.71	0.839	33.15	0.877

registration and an extra high quality reference for model training. These advantages contribute to superior performance of MIDPI-trained DCNN models when the inference is carried out on screen images in the MIDPI dataset. A tantalizing question is whether the MIDPI-trained model can still keep its competitive edge when being applied to real world images. After all, images displayed on monitor are not the same as those captured in real world. Can the monitor-induced dual-reference data offset the nuance differences between the screen-displayed and real world images?

To answer the above question, now we compare how a given DCNN SR model can superresolve real LR images, if trained by the MIDPI dataset versus if trained by other competing datasets. The synthetic BD dataset is still selected as a competitor. We choose two DCNN SR models (EDSR and RCAN) in the comparison study, because they are the two best performers in Table. II. Since for real LR images there are no ground truth images, we cannot compute PSNR and SSIM. Instead, we compare in Fig. 11 the output images of EDSR and RCAN after the networks are trained by the MIDPI dataset versus trained by the BD dataset. As shown, for

real images captured by three different cameras, both MIDPI-trained EDSR and MIDPI-trained RCAN reproduce sharper edges and details than the models trained on the synthesized dataset. This provides empirical evidence for the generalization capability of the MIDPI datasets from screen to real world images.

In the previous experiment of Fig. 11, the realistic images for inference and the training images are captured by the same DSLR cameras. Next we check what if the inference images and training images are captured by different cameras. We add in the comparison of Chen *et al.*'s dataset [25] and Cai *et al.*'s camera-captured SR training dataset [26], and retrain the RCAN models by the LR~HR images ($\times 4$) of these datasets. In Chen *et al.*'s dataset, similar to our MIDPI, the realistic LR~HR image pairs are collected under a controllable experimental environment. They printed 100 postcards and captured them twice with lenses of different focal lengths. Their image pairs are aligned by only using SIFT features. Cai *et al.*'s [26] collected LR~HR image pairs by capturing real-world static scenes.

In Fig. 12, the test LR images are from Cai's dataset [26]. The SR results are produced by three RCAN models trained by Chen's dataset, Cai's dataset and MIDPI dataset separately. As this figure shows, MIDPI trained model outperforms the competitors by achieving sharper edges. In contrast, Chen's dataset [25] and Cai's dataset [26] perform badly as they cannot register the image pairs precisely and lack an additional reference which provides high frequency information. Fig. 13 presents the SR inference results on images of the two smartphone cameras (iPhone 7plus and iPhone 11). The four



Fig. 13: SR results ($\times 4$) of real-world images captured by iPhone 7plus and iPhone 11.

RCAN models are trained by BD dataset, Chen's dataset [25], Cai's training dataset [26] and MIDPI, respectively. The experimental results show that the MIDPI-trained SR model recovers sharper and cleaner details with less artifacts than the other three models, when they are applied to novel cameras whose images are unseen during the training. All these test images are outside of our MIDPI-trained dataset. These experiments offer additional empirical evidence for the robustness of the MIDPI training data generation strategy.

D. Ablation study of digital files

To verify the advantages of the strategy by training SR models with digital HR images, we compare RCAN models trained on the proposed MIDPI dataset w/ and w/o the digital HR reference \mathcal{Y}_i . As shown in Fig. 14, the results of the model without \mathcal{Y}_i have some wierd high-frequency artifacts around the edges. In contrast, the digital HR images trained model can produce clear results meanwhile erasing the unintended high-frequency blemishes. These improvement demonstrates the

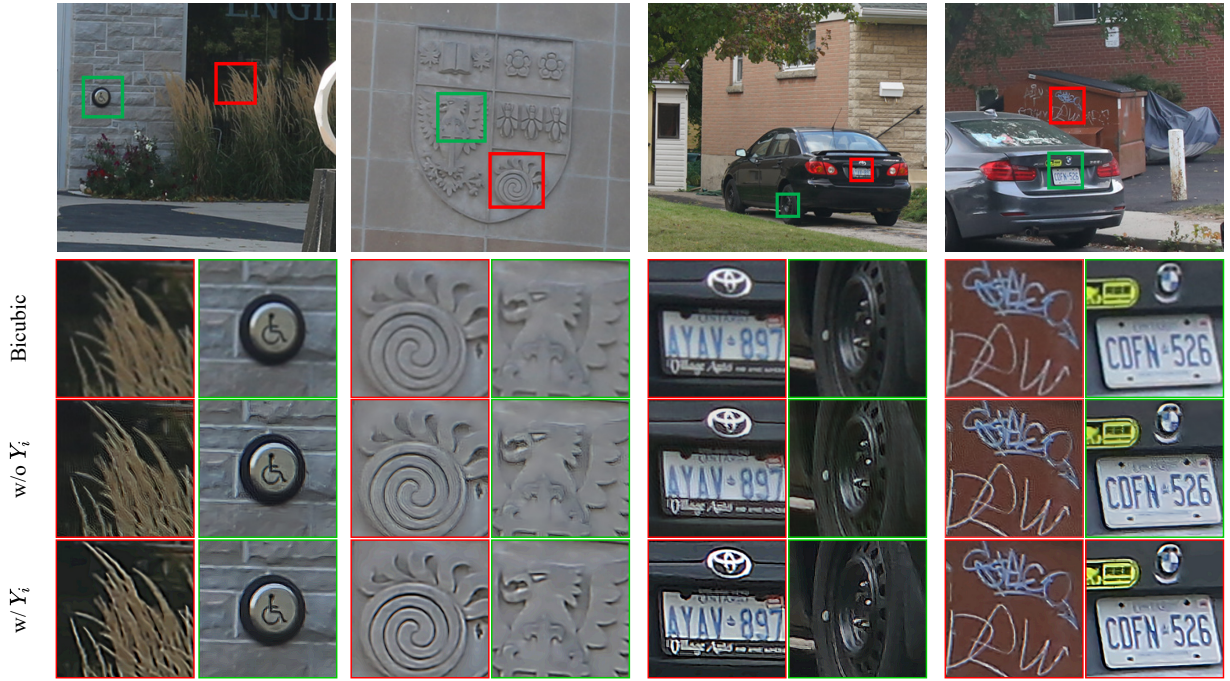


Fig. 14: Comparison of SR results with and without digital HR images for supervision. Zoom in for better view.

effectiveness of our proposed dual reference for SR model training. With the dual reference strategy, the unintended artifacts of captured image pairs can be restrained, while the super high quality reference can promote the performance of the trained SR models.

E. Cross-camera evaluation

CNN methods are very sensitive to nuance differences between the training and inference data. Therefore, a CNN SR method will suffer performance losses if it is trained by images taken by one camera but is used to restore images taken by another. To evaluate the immunity of such performance losses, we conduct the following cross-camera experiments. We train three RCAN models by three camera-specific MIDPI datasets respectively, and then test them on images drawn from all the three MIDPI datasets that are unseen in the training. Table. III reports the PSNR and SSIM values of the experimental results. An interesting observation is that the performance decays between two different cameras, as shown in the first row of the Table. III, even if they are made by the same manufacturer (0.37 dB gap between Sony Nex-6 and Sony Alpha-a7RII). Moreover, the performance gap between two cameras from different manufacturer is bigger (e.g., 0.60 dB gap between Sony Nex-6 and Canon 5D-MarkIII). As illustrated in the last row of the Table. III, both models trained by Sony Nex-6 MIDPI dataset and Canon 5D-MarkIII MIDPI dataset are not nearly as good as the Sony Alpha-a7RII MIDPI trained model. These observations suggest that for best performance the DCNN SR model trained by images captured by a camera should be applied to images of the same camera. Thanks to the high data collection throughput of the MIDPI system, Our MIDPI system can be easily employed to collect a mass of realistic SR image pairs. In our experiment, it only takes 4

TABLE III: Average PSNR/SSIM ($\times 4$) for cross-camera evaluation. All models are of RCAN structure.

Camera	Sony Nex-6	Canon 5D-MarkIII	Sony Alpha-a7RII
Sony Nex-6	33.15/0.877	32.55/0.809	32.78/0.893
Canon 5D-MarkIII	31.71/0.862	33.24/0.853	31.90/0.872
Sony Alpha-a7RII	32.14/0.868	32.17/0.801	33.21/0.903

hours (about 500 image pairs per hour) to collect 1800 image pairs for three cameras. The size of MIDPI dataset is much larger than existing realistic SR datasets. With the proposed MIDPI system, one can simply collect training datasets for each of the intended cameras and build a camera-specific DCNN SR model for it.

V. CONCLUSION

The proposed MIDPI generation of training data for deep learning based superresolution offers unprecedented alignment accuracy between LR and HR image pairs captured by a camera. This unique advantage contributes to superior performance of MIDPI-trained DCNN SR models over the same models trained by other LR~HR datasets. In addition, MIDPI system can collect sufficient paired data under lab conditions. It makes it easy to deploy specific SR models for any type of digital camera and real scene. The proposed unprecedented idea by using dual reference for training SR models, breaking through limitation of the used camera for realistic SR data collection. Our abundant experiments reveal the great effectiveness of our MIDPI dataset for CNN super-resolution models.

REFERENCES

- [1] W. T. Freeman, E. C. Pasztor, and O. T. Carmichael, "Learning low-level vision," *International journal of computer vision*, vol. 40, no. 1, pp. 25–47, 2000. 1

- [2] R. Timofte, V. De, and L. V. Gool, "Anchored neighborhood regression for fast example-based super-resolution," in *2013 IEEE International Conference on Computer Vision*, 2013, pp. 1920–1927. 1
- [3] G. Freedman and R. Fattal, "Image and video upscaling from local self-examples," *ACM Trans. Graph.*, vol. 28, no. 3, pp. 1–10, 2010. 1
- [4] D. Glasner, S. Bagon, and M. Irani, "Super-resolution from a single image," in *2009 IEEE 12th International Conference on Computer Vision*, 2009, pp. 349–356. 1
- [5] J. Yang, Z. Lin, and S. Cohen, "Fast image super-resolution based on in-place example regression," in *2013 IEEE Conference on Computer Vision and Pattern Recognition*, 2013, pp. 1059–1066. 1
- [6] J.-B. Huang, A. Singh, and N. Ahuja, "Single image super-resolution from transformed self-exemplars," in *Proceedings of the IEEE conference on computer vision and pattern recognition*, 2015, pp. 5197–5206. 1, 3
- [7] J. Yang, J. Wright, T. S. Huang, and Y. Ma, "Image super-resolution via sparse representation," *IEEE transactions on image processing*, vol. 19, no. 11, pp. 2861–2873, 2010. 1
- [8] C. Dong, C. C. Loy, K. He, and X. Tang, "Image super-resolution using deep convolutional networks," *IEEE transactions on pattern analysis and machine intelligence*, vol. 38, no. 2, pp. 295–307, 2015. 1
- [9] C. Ledig, L. Theis, F. Huszár, J. Caballero, A. Cunningham, A. Acosta, A. Aitken, A. Tejani, J. Totz, Z. Wang *et al.*, "Photo-realistic single image super-resolution using a generative adversarial network," in *Proceedings of the IEEE conference on computer vision and pattern recognition*, 2017, pp. 4681–4690. 1
- [10] Y. Zhang, K. Li, K. Li, L. Wang, B. Zhong, and Y. Fu, "Image super-resolution using very deep residual channel attention networks," in *Proceedings of the European Conference on Computer Vision (ECCV)*, 2018, pp. 286–301. 1
- [11] Y. Blau, R. Mechrez, R. Timofte, T. Michaeli, and L. Zelnik-Manor, "The 2018 pirm challenge on perceptual image super-resolution," in *Proceedings of the European Conference on Computer Vision (ECCV)*, 2018, pp. 0–0. 1
- [12] R. Timofte, S. Gu, J. Wu, and L. Van Gool, "Ntire 2018 challenge on single image super-resolution: Methods and results," in *Proceedings of the IEEE conference on computer vision and pattern recognition workshops*, 2018, pp. 852–863. 1, 7
- [13] C. Dong, C. C. Loy, K. He, and X. Tang, "Image super-resolution using deep convolutional networks," *IEEE transactions on pattern analysis and machine intelligence*, vol. 38, no. 2, pp. 295–307, 2015. 1
- [14] W. Shi, J. Caballero, F. Huszár, J. Totz, A. Aitken, R. Bishop, D. Rueckert, and Z. Wang, "Real-time single image and video super-resolution using an efficient sub-pixel convolutional neural network," 06 2016. 1
- [15] B. Lim, S. Son, H. Kim, S. Nah, and K. Mu Lee, "Enhanced deep residual networks for single image super-resolution," in *Proceedings of the IEEE conference on computer vision and pattern recognition workshops*, 2017, pp. 136–144. 1, 7
- [16] Y. Zhang, Y. Tian, Y. Kong, B. Zhong, and Y. Fu, "Residual dense network for image super-resolution," in *Proceedings of the IEEE conference on computer vision and pattern recognition*, 2018, pp. 2472–2481. 1
- [17] Y. Zhang, K. Li, K. Li, L. Wang, B. Zhong, and Y. Fu, "Image super-resolution using very deep residual channel attention networks," in *Proceedings of the European Conference on Computer Vision (ECCV)*, 2018, pp. 286–301. 1, 7
- [18] F. Yang, H. Yang, J. Fu, H. Lu, and B. Guo, "Learning texture transformer network for image super-resolution," in *Proceedings of the IEEE/CVF Conference on Computer Vision and Pattern Recognition*, 2020, pp. 5791–5800. 1
- [19] J. Kim, J. K. Lee, and K. M. Lee, "Deeply-recursive convolutional network for image super-resolution," in *2016 IEEE Conference on Computer Vision and Pattern Recognition (CVPR)*, 2016, pp. 1637–1645. 1
- [20] J. Kim, J. Kwon Lee, and K. Mu Lee, "Accurate image super-resolution using very deep convolutional networks," in *Proceedings of the IEEE conference on computer vision and pattern recognition*, 2016, pp. 1646–1654. 1, 7
- [21] J. Johnson, A. Alahi, and L. Fei-Fei, "Perceptual losses for real-time style transfer and super-resolution," in *European conference on computer vision*. Springer, 2016, pp. 694–711. 1
- [22] C. Ledig, L. Theis, F. Huszár, J. Caballero, A. Cunningham, A. Acosta, A. Aitken, A. Tejani, J. Totz, Z. Wang *et al.*, "Photo-realistic single image super-resolution using a generative adversarial network," in *Proceedings of the IEEE conference on computer vision and pattern recognition*, 2017, pp. 4681–4690. 1, 7
- [23] M. S. Sajjadi, B. Scholkopf, and M. Hirsch, "Enhancenet: Single image super-resolution through automated texture synthesis," in *Proceedings of the IEEE International Conference on Computer Vision*, 2017, pp. 4491–4500. 1
- [24] X. Wang, K. Yu, S. Wu, J. Gu, Y. Liu, C. Dong, Y. Qiao, and C. Change Loy, "Esrgan: Enhanced super-resolution generative adversarial networks," in *Proceedings of the European Conference on Computer Vision (ECCV) Workshops*, September 2018. 1
- [25] C. Chen, Z. Xiong, X. Tian, Z.-J. Zha, and F. Wu, "Camera lens super-resolution," 2019. 1, 3, 9, 10
- [26] J. Cai, H. Zeng, H. Yong, Z. Cao, and L. Zhang, "Toward real-world single image super-resolution: A new benchmark and a new model," in *Proceedings of the IEEE International Conference on Computer Vision*, 2019. 1, 2, 3, 4, 7, 9, 10
- [27] X. C. Zhang, Q. Chen, R. Ng, and V. Koltun, "Zoom to learn, learn to zoom," 2019. 1, 2, 3, 4, 7
- [28] M. Bevilacqua, A. Roumy, C. Guillemot, and M. L. Alberi-Morel, "Low-complexity single-image super-resolution based on nonnegative neighbor embedding," 2012. 3
- [29] E. M. Zeyde Roman and P. Matan, "On single image scale-up using sparse-representations," in *International conference on curves and surfaces*. Springer, 2010, pp. 711–730. 3
- [30] R. Timofte, E. Agustsson, L. Van Gool, M.-H. Yang, and L. Zhang, "Ntire 2017 challenge on single image super-resolution: Methods and results," in *Proceedings of the IEEE conference on computer vision and pattern recognition workshops*, 2017, pp. 114–125. 3
- [31] W. Dong, L. Zhang, G. Shi, and X. Li, "Nonlocally centralized sparse representation for image restoration," *IEEE transactions on Image Processing*, vol. 22, no. 4, pp. 1620–1630, 2012. 3
- [32] X. Xu, Y. Ma, and W. Sun, "Towards real scene super-resolution with raw images," *2019 IEEE/CVF Conference on Computer Vision and Pattern Recognition (CVPR)*, pp. 1723–1731, 2019. 3
- [33] J. Yoo, N. Ahn, and K.-A. Sohn, "Rethinking data augmentation for image super-resolution: A comprehensive analysis and a new strategy," 04 2020. 3
- [34] D. S. Jeon, S.-H. Baek, I. Choi, and M. H. Kim, "Enhancing the spatial resolution of stereo images using a parallax prior," in *Proceedings of the IEEE Conference on Computer Vision and Pattern Recognition*, 2018, pp. 1721–1730. 3
- [35] L. Wang, Y. Wang, Z. Liang, Z. Lin, J. Yang, W. An, and Y. Guo, "Learning parallax attention for stereo image super-resolution," in *Proceedings of the IEEE Conference on Computer Vision and Pattern Recognition*, 2019, pp. 12250–12259. 3
- [36] M. Fritsche, S. Gu, and R. Timofte, "Frequency separation for real-world super-resolution," 10 2019, pp. 3599–3608. 3
- [37] Y. Yuan, S. Liu, J. Zhang, Y. Zhang, C. Dong, and L. Lin, "Unsupervised image super-resolution using cycle-in-cycle generative adversarial networks," in *Proceedings of the IEEE Conference on Computer Vision and Pattern Recognition Workshops*, 2018, pp. 701–710. 3
- [38] A. Bulat, J. Yang, and G. Tzimiropoulos, "To learn image super-resolution, use a gan to learn how to do image degradation first," in *Computer Vision – ECCV 2018*. Cham: Springer International Publishing, 2018, pp. 187–202. 3
- [39] C. Qu, D. Luo, E. Monari, T. Schuchert, and J. Beyerer, "Capturing ground truth super-resolution data," in *2016 IEEE International Conference on Image Processing (ICIP)*, 2016, pp. 2812–2816. 3
- [40] T. Köhler, M. Bätz, F. Naderi, A. Kaup, A. Maier, and C. Riess, "Toward bridging the simulated-to-real gap: Benchmarking super-resolution on real data," *IEEE Transactions on Pattern Analysis and Machine Intelligence*, vol. 42, no. 11, pp. 2944–2959, 2020. 3
- [41] D. G. Lowe, "Distinctive image features from scale-invariant keypoints," *International journal of computer vision*, vol. 60, no. 2, pp. 91–110, 2004. 3, 5
- [42] Z. Zhang, "A flexible new technique for camera calibration," *IEEE Transactions on pattern analysis and machine intelligence*, vol. 22, no. 11, pp. 1330–1334, 2000. 4
- [43] H. Bay, T. Tuytelaars, and L. Van Gool, "Surf: Speeded up robust features," in *European conference on computer vision*. Springer, 2006, pp. 404–417. 5
- [44] H. Foroosh, J. B. Zerubia, and M. Berthod, "Extension of phase correlation to subpixel registration," *IEEE transactions on image processing*, vol. 11, no. 3, pp. 188–200, 2002. 6
- [45] M. Guizar-Sicairos, S. Thurman, and J. Fienup, "Efficient subpixel image registration algorithms," *Optics letters*, vol. 33, pp. 156–8, 02 2008. 6
- [46] D. P. Kingma and J. Ba, "Adam: A method for stochastic optimization," *arXiv preprint arXiv:1412.6980*, 2014. 7